Extreme output sensitivity to subwavelength boundary deformation in microcavities

Li Ge,[1,*] Qinghai Song,[2] Brandon Redding,[3] and Hui Cao[3,†]
[1]*Department of Electrical Engineering, Princeton University, Princeton, New Jersey 08544, USA*
[2]*Department of Electronic and Information Engineering, Shenzhen Graduate School, Harbin Institute of Technology, Shenzhen 518055 China*
[3]*Department of Applied Physics, Yale University, New Haven, Connecticut 06520-8482, USA*
(Received 25 July 2012; published 22 February 2013)

We demonstrate a generic and robust mechanism that leads to an extreme output sensitivity to a deep subwavelength boundary perturbation in wavelength-scale microcavities. A deformation of the cavity boundary on the order of ten-thousandth of a wavelength may flip the output directions by 180°, corresponding to a variation of 0.1 nm for a 1-μm-radius cavity. Our analysis based on a perturbation theory reveals that such tiny structural change can cause a strong mixing of nearly degenerate cavity resonances with different angular momenta, and their interference is greatly enhanced to have a radical influence on the far-field pattern. Our finding opens the possibility of utilizing carefully designed wavelength-scale microcavities for fast beam steering and high-resolution detection.

DOI: 10.1103/PhysRevA.87.023833 PACS number(s): 42.55.Sa, 05.45.Mt, 42.25.−p

I. INTRODUCTION

Optical microcavities have a wide range of applications from coherent light sources in integrated photonic circuits to cavity quantum electrodynamics, single-photon emitters, and biochemical sensors [1,2]. For example, ultrahigh quality (Q) factor microcavities have demonstrated extraordinarily high sensitivity in detection of single molecules and viruses [3–5]. The extremely long lifetime of whispering-gallery modes in circular microcavities greatly enhances the interaction of the circulating light with a tiny perturbation on the cavity boundary, which leads to a shift of resonant frequencies. However, the long lifetime also means a slow response of the sensors, limiting the sampling frequency. Moreover, the ultrahigh Q is very fragile against surface roughness, which is common to semiconductor microdisks and -rings, and the cavity size cannot be reduced to wavelength scale due to Q degrading.

In this article we present a fundamentally different scheme to achieve an extremely sensitive response to a perturbation on the cavity boundary. By exploring deformation induced coupling between nearly degenerate cavity resonances, we show that a variation on the order of 0.1 nm along the boundary of a 1-μm-radius disk can flip the output direction by 180°, which is much more dramatic than the relative frequency shift ($\Delta\omega/\omega \ll 1$) of the current microcavity sensors. Our scheme is applicable to wavelength-scale microcavities with relatively low Q factors, and it allows fast response and is robust against the surface roughness. Moreover, it provides a means of rapid steering of microcavity emission with low-energy consumption, which has important applications for microlasers and single-photon emitters.

Previous studies have shown that cavity deformation can strongly modify the intracavity ray dynamics and the output directionality [6–16]. The intracavity ray dynamics becomes (partially) chaotic for a large deformation from an integrable cavity shape, and the emergence of unstable manifolds of distinct geometries lead to dramatically different emission patterns from similarly deformed microlasers [11]. For a small deformation from a circle or sphere [7,17–22], evanescent tunneling is dominant over refractive escape, and it can be highly directional due to nonperturbative phase-space structures in the intracavity ray dynamics. All these studies were performed in the semiclassical regime, where the cavity size R is much larger than the wavelength λ. As such, the variation of the boundary, though small compared to R, is comparable to or even larger than the wavelength. The same variation of the boundary as a fraction of R becomes much smaller than the wavelength in the wave regime, where $R \to \lambda$ [23–25]. Thus one would have expected the deformation to have a much weaker influence, for example, on the output directionality and intracavity field distribution. While the intracavity field distribution is indeed insensitive to the deformation in the wavelength regime, the output directionality is surprisingly much more sensitive than the prediction of the intracavity ray dynamics, which we attribute to deformation induced coupling.

Mode coupling in microcavities has been extensively studied [26–29], but the extreme sensitivity we report here has never been found. Both numerical simulation and perturbation theory show that the ultrahigh sensitivity is *unique* for the output directionality and absent in all other properties of the resonances, such as the frequencies, Q factors, and intracavity field patterns mentioned above. Thanks to the generality of the wave equations, our findings can be applied to other types of waves such as polaritons and acoustic waves.

Below we first present the numerical results that show the dramatic sensitivity of the output directionality on the boundary deformation in Sec. II, followed by the analysis based on a perturbation theory that reveals the underlining mechanism in Sec. III. In Sec. IV, we discuss the generality of our approach and its potential applications.

II. OUTPUT SENSITIVITY: NUMERICAL SIMULATIONS

Although our results are relevant for a variety of deformed cavities, we present below a simple example of a

*lge@princeton.edu
†hui.cao@yale.edu

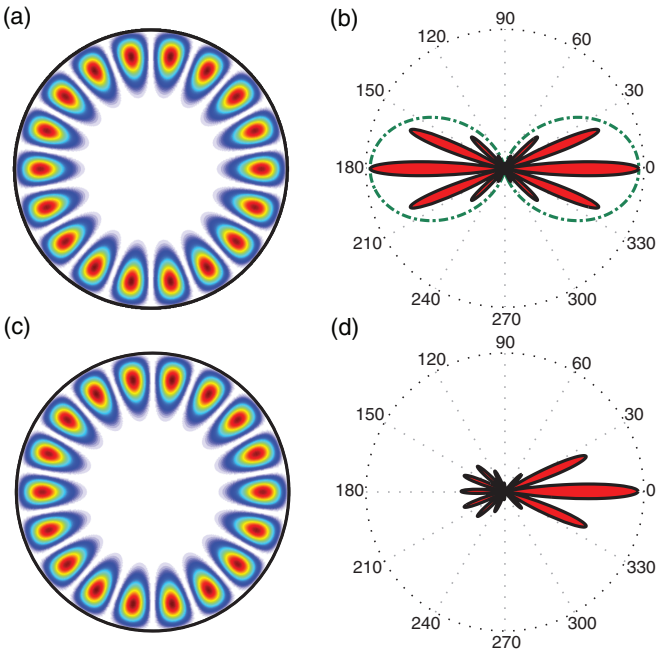

FIG. 1. (Color online) Intracavity field distribution (a) and far-field intensity pattern (b) of mode 1 at $kR = 4.387 - i\,1.809 \times 10^{-5}$ in a quadrupole cavity with $R = 1\ \mu$m, $\epsilon_2 = -0.01$, $\epsilon_3 = 0$, and $n = 3$. Black solid contour in (b) represents the far field obtained from the second-order perturbation theory, which agrees almost exactly with the numerical data (red shadow). Green dash-dotted contour shows the envelope $1 + \cos(2\theta)$. (c), (d) Same as (a), (b), but the cavity is now sightly perturbed with $\epsilon_3 = 10^{-4}$. The resonance shifts slightly to $kR = 4.387 - i2.039 \times 10^{-5}$.

two-dimensional dielectric cavity slightly deformed from a circle. The deformation is characterized by harmonic perturbation of the boundary, $\rho(\theta) = R[1 + \epsilon_2 \cos(2\theta) + \epsilon_3 \cos(3\theta)]$ in the polar coordinates, where $|\epsilon_2|, |\epsilon_3| \ll 1$. A small dipolar term $(\epsilon_1 \cos\theta)$ mostly leads to a lateral shift of the cavity, and it can be eliminated by choosing a proper origin of the coordinate system. Because the cavity has reflection symmetry with respect to the horizontal axis, the cavity resonances have either even parity or odd parity about $\theta = 0^\circ$. Below we consider the even-parity modes, and the analysis of the odd-parity modes is similar. Using a scattering matrix approach [30,31] we calculate the cavity resonant frequencies and Q factors of transverse electric (TE) modes (electric field parallel to the disk plane), which are most common in microdisk lasers. The dramatic boundary sensitivity to be discussed below also exists for transverse magnetic (TM) modes.

We first consider slightly deformed quadrupolar cavities with $\epsilon_2 = -0.01$ and ϵ_3 set to zero. Series of quasi-whispering-gallery mode (WGM) can be found, and Fig. 1(a) shows one at $\mathrm{Re}[kR] \approx 4.387$ (mode 1). Its output is bidirectional towards $\theta = 0^\circ, 180^\circ$ [Fig. 1(b)], which we analyze in the polar coordinates together with the intracavity field:

$$\psi^{(m)}(r,\theta) = \begin{cases} \sum_p A_p J_p(nkr)\cos(p\theta), & r < \rho(\theta), \\ \sum_p B_p H_p(kr)\cos(p\theta), & r > \rho(\theta). \end{cases} \quad (1)$$

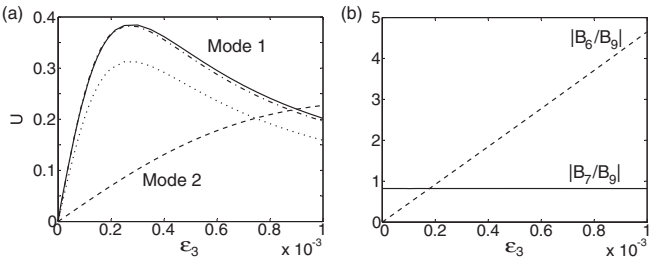

FIG. 2. (a) U versus ϵ_3 for modes 1 (solid line) and 2 (dashed line) in Fig. 5(a). First-order (dotted line) and second-order (dash-dotted line) perturbation results for mode 1 are also shown. (b) Ratio of Hankel coefficients $|B_7/B_9|$ (solid line) and $|B_6/B_9|$ (dashed line) of mode 1 as a function of ϵ_3.

$J_p(nkr)$, $H_p(kr)$ are the pth order Bessel function and outgoing Hankel function, respectively. $A_p(B_p)$ will be referred to as the Bessel (Hankel) coefficients inside (outside) the cavity. Since $|\epsilon_2| \ll 1$, each WGM has a dominant angular momentum m inside the cavity, and for mode 1 $m = 9$. The quadrupolar deformation $\epsilon_2 \cos(2\theta)$ scatters light from m to $m \pm 2$. Since the $m + 2$ component is more tightly confined within the cavity, the far-field pattern is largely determined by the interference of the m and $m - 2$ components [Fig. 3(b)]. When the latter two have almost equal amplitudes, their beating gives rise to an envelope function $1 + \cos(2\theta)$, which agrees well with that of mode 1.

To alter the output directionality strongly, a $\epsilon_3 \cos(3\theta)$ deformation is added to $\rho(\theta)$ which generates additional $m \pm 3$ components, with $m - 3$ stronger than $m + 3$ outside the cavity. Consequently, the dominant Hankel coefficients are $m, m-2, m-3$ as shown in Fig. 3(d) for mode 1 at $\epsilon_3 = 10^{-4}$; they not only have comparable amplitudes but also similar phases. Since $\cos(6\theta)$ is symmetric about the vertical axis while $\cos(7\theta)$ and $\cos(9\theta)$ are antisymmetric, it interferes with the other two constructively along $\theta = 0^\circ$ and destructively along $\theta = 180^\circ$, creating the directional emission shown in Fig. 1(d). Note that by changing the sign of ϵ_3, the output direction of mode 1 is reversed, since the cavity changes to its mirror image about the vertical axis, i.e., $\rho(\pi - \theta) = R[1 + \epsilon_2 \cos(2\theta) - \epsilon_3 \cos(3\theta)]$.

Below we measure the output direction by $U \equiv \int_0^{2\pi} d\theta\, I(\theta) \cos\theta$, where $I(\theta)$ is the normalized far-field intensity satisfying $\int_0^{2\pi} d\theta\, I(\theta) = 1$. U is zero for isotropic or bidirectional emission, and positive (negative) for directional emission along $\theta = 0^\circ$ (180°). U of mode 1 rapidly increases to its maximum of 0.39 at $\epsilon_3 \simeq 2.7 \times 10^{-4}$ [Fig. 2(a)], at which the interference between even and odd angular components is strongest. As ϵ_3 further increases, the increasing amplitude difference between even and odd angular components [see Fig. 2(b)] reduces the interference effect, bringing down the enhanced emission along $\theta = 0^\circ$.

Despite the drastic change of the far-field pattern, the intracavity field distribution remains nearly the same [Fig. 1(c)], because the deformation introduced Bessel coefficient A_6 in mode 1 is much smaller than A_9 [see Fig. 3(c)]. This holds true even when ϵ_3 increases to 10^{-3}, at which B_6 dominates over B_9 and B_7 outside the cavity.

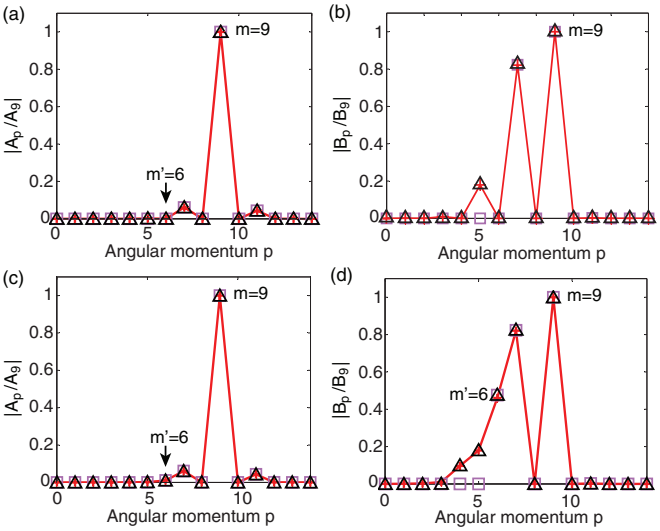

FIG. 3. (Color online) Bessel coefficients inside the cavity (a) and Hankel coefficients outside the cavity (b) of mode 1 at $\epsilon_3 = 0$. Red crosses connected by solid line show the numerical data. Squares and triangles are given by the first- and second-order perturbation theories, respectively. (c), (d) Same as (a), (b), but the cavity is now sightly perturbed with $\epsilon_3 = 10^{-4}$. Note that the increase of $|A_6|$ in (c) is very small compared with that of $|B_6|$ in (d).

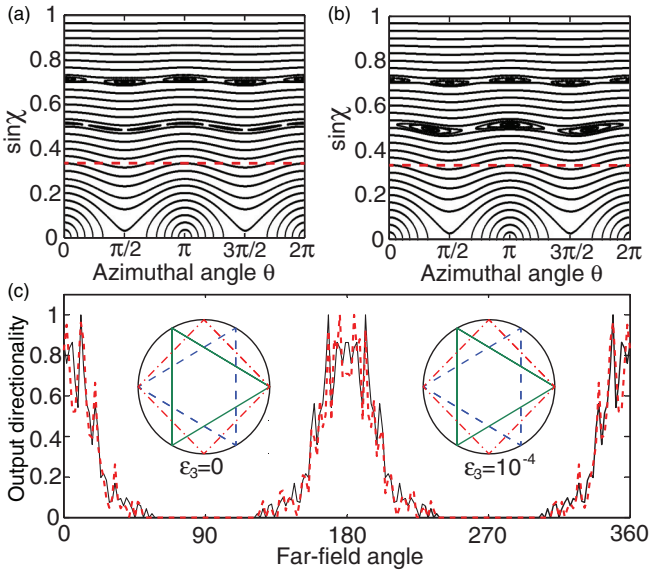

FIG. 4. (Color online) (a) SOS for the intracavity ray dynamics at $\epsilon_3 = 0$. The islands near $\sin\chi = 0.5$ correspond to the left ("◁") and right ("▷") triangular orbits, and the ones near $\sin\chi = 0.7$ correspond to the diamond orbit ("◇"). Red dashed line indicates the critical line, i.e., $\sin\chi = 1/n$. (b) Same as (a) but at $\epsilon_3 = 10^{-4}$. The right triangular orbit becomes unstable. (c) Output directionality obtained by tracing 40 000 random rays uniformly distributed in the SOS above the critical line. The output is collected each time they refract at the boundary. Thin black solid line and thick dashed red line are for $\epsilon_3 = 0$ and 10^{-4}, respectively. Insets: Above-mentioned orbits shown in real space, which display little change with ϵ_3.

III. ORIGIN OF THE OUTPUT SENSITIVITY

The observed boundary sensitivity cannot be accounted for using semiclassical ray dynamics [7,8], in which light is treated as particles undergoing specular reflections at the cavity boundary. In this picture the dynamical properties of light are usually represented by the Poincaré surface of section (SOS), using the positions of rays incident on the boundary (represented by the azimuthal angle θ) and the corresponding angles of incidence χ. As shown in Figs. 4(a) and 4(b), the majority of the SOS remains regular in the presence of a small ϵ_2 and ϵ_3, with unbroken Kolmogorov-Arnold-Moser curves representing the WGM trajectories ($\theta \in [0^\circ, 360^\circ]$). There are a few islands corresponding to stable periodic orbits, including the right ("▷") triangle which becomes unstable when ϵ_3 changes from 0 to 10^{-4}. To investigate its connection to the change of emission directionality, we perform ray tracing which includes the effect of all dynamical structures in the phase space. Figure 4(c) plots the intensities of output rays for $\epsilon_3 = 0^\circ$ and 10^{-4}, which are very similar and peaked at $\theta = 0^\circ, 180^\circ$. This result shows that the stability change of the right triangular orbits is just a coincidence and not related to the dramatic change of the output directionality observed in the actual modes. We note that the ray model applies in the semiclassical regime, where the same value of ϵ_3 stands for a boundary perturbation ($\sim\epsilon_3 R$) much larger than the wavelength and where a stronger effect would have been anticipated.

Another way to understand the bidirectional output at $\epsilon_3 = 0$ intuitively is from the curvature of the boundary. It is highest at $\theta = 90^\circ, 270^\circ$, and the evanescent tunneling at these places is also strongest, giving rise to the bidirectional emission observed. This picture, however, fails when ϵ_3 becomes nonzero. For example, the highest curvature points only shift about 1° at $\epsilon_3 = 10^{-4}$, which cannot explain the dramatic change of the output directionality we observe.

The failure of the two approaches above to capture the output sensitivity highlights the wave nature of the observed radical response and implies a strong mechanism that has not been explored before. To identify this mechanism, we examine the cavity modes in the vicinity of mode 1, which form a higher-Q and a lower-Q series [Fig. 5(a)]. A correlation is observed between the output direction of the higher-Q mode and its frequency spacing to the nearby lower-Q mode: mode 1 has the largest U at $\epsilon_3 = 10^{-4}$ and its distance to its quasidegenerate partner (mode $1'$) is also the shortest. Mode $1'$ has a dominant angular momentum $m' = 6$, which appears in mode 1 when $\epsilon_3 \neq 0$. These observations suggest a coupling between modes 1 and $1'$. Recent studies [23,32] show that a higher-Q mode can acquire the directional emission of a lower-Q mode via coupling. However, this scenario does not take place here; mode $1'$ emits more or less symmetrically along $\theta = 0^\circ, 180^\circ$ (see Fig. 6). In addition, the relative changes of the complex frequencies of the coupled modes (e.g., 1 and $1'$), which are normally used to determine mode coupling, are only of the order 10^{-7}. Thus what we presented here is quite an untypical scenario of mode coupling.

To understand the relation of mode coupling and the boundary sensitivity, we adopt a perturbation theory [33–36] to the TE modes. Since the cavity is slightly deformed from a circle, we use the resonances k_0 of a circular cavity of radius R as the unperturbed basis and treat the deformation

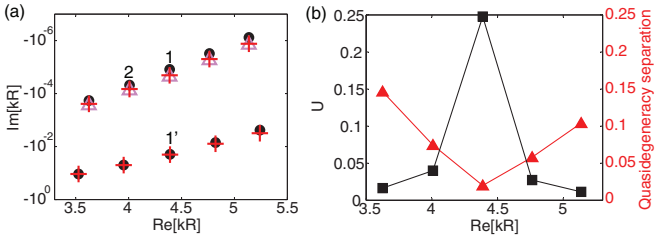

FIG. 5. (Color online) (a) Complex resonant frequency kR (red crosses) of a cavity with $R = 1\ \mu$m, $\epsilon_2 = -0.01$, $\epsilon_3 = 10^{-4}$, and $n = 3$. Triangles show the second-order perturbation results for the high-Q series. The corresponding resonances in a circular cavity of the same R are marked by black dots. (b) Output direction U of the high-Q resonances (squares) and their distances to the nearest low-Q resonances in the complex frequency plane (triangles) versus Re$[kR]$ of the high-Q modes.

$\epsilon_2 \cos(2\theta) + \epsilon_3 \cos(3\theta) \equiv \epsilon f(\theta)/R$ as the perturbation. k_0 are determined by the boundary condition for TE modes in a circular cavity, i.e.,

$$T_m(k_0R) \equiv \frac{J'_m(nk_0R)}{nJ_m(nk_0R)} - \frac{H'_m(k_0R)}{H_m(k_0R)} = 0. \tag{2}$$

The resonant frequency in the deformed cavity can be expanded as $k = k_0 + k_1\epsilon + k_2\epsilon^2 + O(\epsilon^3)$. For convenience, we rewrite $A_p = a_p/J_p(nkR)$, $B_p = (a_p + b_p)/H_p(kR)$, and normalize $\psi(\vec{r})$ by scaling the dominant a_p to unity. In the Appendix we show that all $a_{p\neq m}$ and b_p are at least of order ϵ^1; thus we define $a_{p\neq m} \equiv \alpha_p\epsilon + \beta_p\epsilon^2 + O(\epsilon^3)$ and $b_p \equiv \mu_p\epsilon + \gamma_p\epsilon^2 + O(\epsilon^3)$. By expanding the TE boundary conditions to ϵ^2 around $r = R, k = k_0$, we find the corrections to the resonant frequency k as well as the coefficients a_p and b_p.

With the second-order corrections $\beta_{p\neq m}$ and γ_p given in the Appendix, the perturbation theory reproduces the numerical results nicely (Figs. 1, 2, and 5). In fact, the essence of the extreme output sensitivity is already well captured by the first-order corrections,

$$\alpha_{p\neq m} = \frac{1}{T_p}\left[k_0RS_m\left(\frac{H'_p}{H_p} - \frac{H'_m}{H_m}\right) - T'_m\right]F_{pm}, \tag{3}$$

$$\mu_p = k_0RS_mF_{pm}, \tag{4}$$

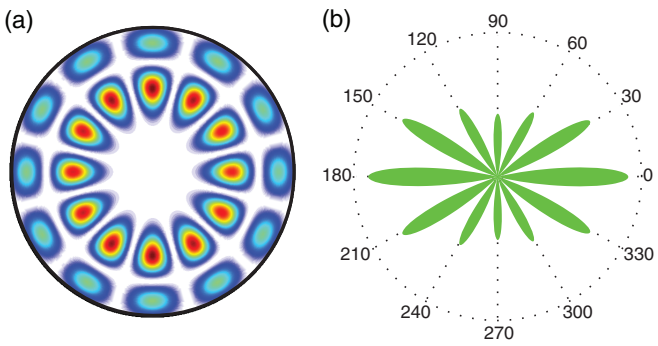

FIG. 6. (Color online) Intracavity field distribution (a) and far-field intensity pattern (b) of a low-Q resonance [mode 1′ in Fig. 5(a)] at $k'R = 4.391 - i2.019 \times 10^{-2}$ with $\epsilon_3 = 10^{-4}$.

as shown in Fig. 2(b). We have dropped the arguments of the Bessel and Hankel functions and defined $F_{pm} \equiv c_p \int_0^{2\pi} f(\theta)\cos(p\theta)\cos(m\theta)d\theta/2\pi$ R $(c_p = 2 - \delta_{p,0})$ and $S_p(x) \equiv nJ'_p(nx)/J_p(nx) - H'_p(x)/H_p(x)$.

The presence of another WGM k'_0R with a dominant angular momentum m' in close vicinity of k_0R implies that $T_{m'}(k_0R) \approx T_{m'}(k'_0R) = 0$. When this occurs, the m' component in $\psi^{(m)}(r,\theta)$ is much enhanced via $\alpha_{m'}$, since $T^{-1}_{m'}(k_0R) \gg 1$. This large prefactor amplifies the small boundary perturbation of $\cos(m - m')\theta$, especially when the m' component is leakier $(m' < m)$ and has a strong influence on the field outside the cavity. For example, the unperturbed WGMs corresponding to modes 1 and 1′ are $k_0R = 4.388 - i1.226 \times 10^{-5}$ with $m = 9$ and $k'_0R = 4.391 - i1.153 \times 10^{-2}$ with $m' = 6$. The factor $|T^{-1}_{m'}(k_0R)| = 7.930$ is much larger than its typical value in the absence of quasidegeneracy. As a result, $\alpha_{m'}$ increases rapidly with $F_{mm'} = \epsilon_3/2$; so does $B_{m'}$ with respect to B_m. The weaker output sensitivity of the other higher-Q modes in Fig. 5(a), e.g., mode 2 [see Fig. 2(b)], can also be understood; their wider separation from the nearest lower-Q mode leads to a smaller enhancement factor $|T^{-1}_{m'}(k_0R)|$. We note that the first-order correction to the resonance, $k_1 = -\epsilon k_0F_{mm}$, vanishes unless $f(\theta)$ changes the average radius (i. e., $\int f(\theta)d\theta \neq 0$), assuming that $f(\theta)$ does not contain the $2mth$-order harmonic perturbation $\cos(2m\theta)$. More importantly, it does not contain the quasi-degeneracy enhancement factor $T^{-1}_{m'}(k_0R)$. Thus the frequency and Q-factor do not show a radical response to the deformation, and the second order treatment is needed to capture the shift of the resonances [Fig. 5(a)].

Note that although $\alpha_{m'}$ also appears in the Bessel coefficient $A_{m'}$, $|A_{m'}/A_m|$ increases much more slowly due to the much smaller factor $|J_{m'}(nkR)/J_m(nkR)|$ compared with $|H_{m'}(kR)/H_m(kR)|$ in $|B_{m'}/B_m|$, which explains the almost identical intracavity field distribution, while the output directionality changes dramatically with ϵ_3.

Another important factor for the extreme sensitivity is the phase of $\alpha_{m'}$, which differs from $a_m(\equiv 1)$ by $\pi/2$ as given by (3). With another relative phase of $\pi/2$ in the asymptotic form of the Hankel function, i.e., $H_p(kr \to \infty) \propto \exp(-ip\pi/2)$, the m' component interferes constructively with the m and $m - 2$ components along $\theta = 0°$ and destructively along $\theta = 180°$.

IV. DISCUSSION AND CONCLUSION

The above analysis based on the perturbation theory reveals that the dramatic response of the output directionality originates from the deformation introduced coupling of quasidegenerate resonances with different angular momenta. This mechanism is general, and the exact shape of the cavity, e.g., the value of ϵ_2 or the presence of higher-order harmonics, is not crucial.

To demonstrate this generality, here we consider another example where the $\cos(2\theta)$ term is absent in the boundary shape. At $\epsilon_3 = 0$ the cavity is circular and the output of all WGMs are isotropic. As shown in Fig. 5(a), modes 1 and 1′ still form a quasidegenerate pair, which leads to a rapid increase of $|B_6|$ with ϵ_3 in mode 1. The beating of $m = 9$ and $m' = 6$ in mode 1 gives rise to a tridirectional output even at

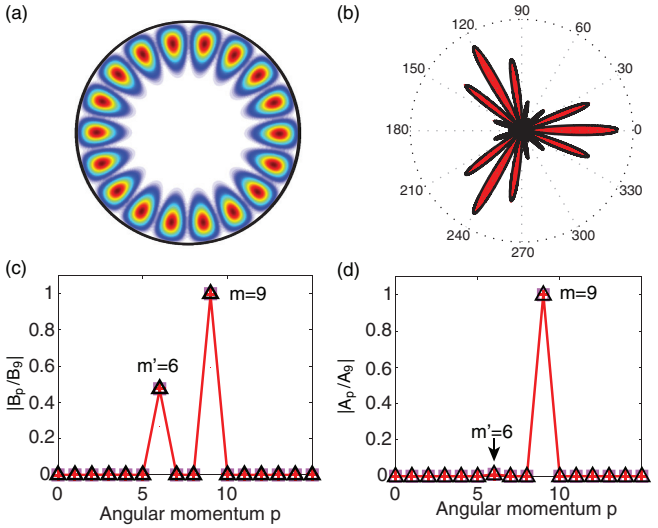

FIG. 7. (Color online) Intracavity field distribution (a), far-field intensity pattern (b), Hankel coefficients (c), and Bessel coefficients (d) of mode 1 at $\epsilon_2 = 0$ and $\epsilon_3 = 10^{-4}$. Other parameters and figure symbols are the same as in Figs. 1 and 3.

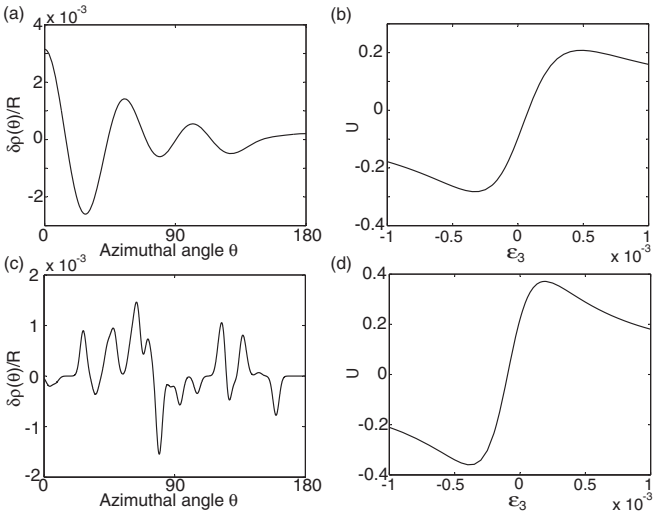

FIG. 8. (a) $\delta\rho(\theta)$ modeled as $R\sum_{p=4}^{8}\delta_p\cos(p\theta)$. In this example $\epsilon_4 = 0.4278\times10^{-3}$, $\epsilon_5 = 0.4814\times10^{-3}$, $\epsilon_6 = 0.8559\times10^{-3}$, $\epsilon_7 = 0.9886\times10^{-3}$, and $\epsilon_8 = 0.3936\times10^{-3}$. (b) U of mode 1 versus ϵ_3 with the boundary roughness shown in (a). (c) $\delta\rho(\theta)$ modeled as random Gaussian bumps and pits. (d) U of mode 1 versus ϵ_3 with the boundary roughness shown in (c). For simplicity we have assumed that $\delta\rho(\theta) = \delta\rho(-\theta)$.

$\epsilon_3 = 10^{-4}$ (see Fig. 7). Note that the value of $|B_6|$ is almost the same as in the previous example [Fig. 3(d)], which is largely determined by the first-order perturbation and all $\epsilon_{p\neq3}$ only contribute weakly.

To further support the generality of our approach, we also consider boundary roughness in the example where $\epsilon_2 = -0.01$. We first treat the boundary roughness as a perturbation with a wide range of angular momenta, i.e., $\delta\rho(\theta) = R\sum_p \delta_p\cos(p\theta)$, in which we have assumed $\delta\rho(\theta) = \delta\rho(-\theta)$ for simplicity. The perturbative contribution of the high-order harmonics ($p \gg 1$) only occurs to Bessel and Hankel coefficients of large angular momenta to the leading order. These components decay rapidly outside the cavity and have little effect on the far field. Thus the far-field intensity pattern only changes with low-order harmonics in the boundary roughness, and we consider $\delta_p(p = 4,5,\ldots,8)$ with a random amplitude up to 10^{-3} when varying ϵ_3. We found that the far-field intensity pattern is modified in the presence of these extra terms, but the sensitivity to ϵ_3 survives. Figure 8(a) shows one example of $\delta\rho(\theta)$, and from Fig. 8(b) we see that U of mode 1 also displays a sensitive dependence on ϵ_3, similar to the case without the surface roughness. In Fig. 8(c) we model the surface roughness in a different way. We include 30 Gaussian bumps and pits randomly distributed around the cavity, with a random amplitude up to $10^{-3}R$ and a full width at half maximum of 5°. Again the sensitivity of U to ϵ_3 can still be observed.

The examples given above emphasize that the key of the dramatic sensitivity of the output directionality is the quasidegeneracy, which has a weak dependence on the small boundary deformation as we have shown using the perturbation theory. As a consequence, quasidegenerate modes can be conveniently identified by examining those of the circular cavity given by Eq. (2). Due to the different spacings of the high-Q and low-Q mode series, accidental quasi-degeneracies occur such as for modes 1 and 1′ in Fig. 5(a). To further reduce the frequency separation of a quasidegenerate pair, one may fine-tune the effective index of a microdisk by changing the disk layer thickness, varying the composition of the material, or using thermal control or carrier injection. Our results can also be directly generalized to terahertz frequency, microwave, and acoustics, due to the scalability of the wave equation.

Our findings offer many practical applications, including a fast and energy efficient way of steering optical signals from microcavities. Using micro-electro-mechanical or optomechanical approaches, one can introduce the proposed cavity deformation and switch the microcavity emission between two or even more desired directions. This can be very useful not only to microlasers but also to single-photon emitters, allowing the delivery of single photons to multiple ports. Utilizing the time reversal of this scheme, i.e., using a passive cavity as a coherent perfect absorber [37,38], one can selectively inject optical signals from different directions into microcavities, again on a fast time scale and with minimal energy cost.

ACKNOWLEDGMENTS

We acknowledge Eugene Bogomolny for bringing to our attention the boundary perturbation theory (Ref. [33]). We also thank Douglas Stone, Remy Dubertrand, Jan Wiersig, Alexander Eberspächer, Hakan Türeci, and Hong Tang for helpful discussions. L.G. acknowledges MIRTHE NSF EEC-0540832. Q.S. acknowledges 2011KFB005 of the State Key Laboratory on Integrated Optoelectronics and NSFC 11204055. B.R. and H.C. acknowledge NSF ECCS-1068642 and ECCS-1128542.

APPENDIX: PERTURBATION THEORY FOR TE MODES

In this section we present the perturbation theory for TE modes in a deformed microdisk cavity, which is more complicated compared with a similar approach for TM modes introduced in Ref. [33]. The "asymmetry" in the boundary conditions for TE modes

$$\psi_<(\rho,\theta)=\psi_>(\rho,\theta),\quad \frac{1}{n^2}\frac{\partial\psi_<}{\partial r}=\frac{\partial\psi_>}{\partial r}, \tag{A1}$$

due to the factor of n^{-2} leads to a more complicated perturbation series and an additional first-order correction. Here $\psi_{<(>)}(r,\theta)$ are the wave function inside (outside) the cavity. By expanding the boundary conditions to $O(\epsilon^2)$ at $r=R$, we obtain

$$\psi_<-\psi_>=-\epsilon f(\theta)\left(\frac{\partial\psi_<}{\partial r}-\frac{\partial\psi_>}{\partial r}\right)-\frac{1}{2}\epsilon^2 f(\theta)^2\left(\frac{\partial^2\psi_<}{\partial r^2}-\frac{\partial^2\psi_>}{\partial r^2}\right), \tag{A2}$$

$$\frac{1}{n^2}\frac{\partial\psi_<}{\partial r}-\frac{\partial\psi_>}{\partial r}=-\epsilon f(\theta)\left(\frac{1}{n^2}\frac{\partial^2\psi_<}{\partial r^2}-\frac{\partial^2\psi_>}{\partial r^2}\right)-\frac{1}{2}\epsilon^2 f(\theta)^2\left(\frac{1}{n^2}\frac{\partial^3\psi_<}{\partial r^3}-\frac{\partial^3\psi_>}{\partial r^3}\right). \tag{A3}$$

Using the ansatz

$$\psi_<(r,\theta)=\sum_p a_p\frac{J_p(nkr)}{J_p(nkR)}\cos(p\theta),\qquad r<\rho(\theta),$$
$$\psi_>(r,\theta)=\sum_p (a_p+b_p)\frac{H_p(kr)}{H_p(kR)}\cos(p\theta),\quad r>\rho(\theta), \tag{A4}$$

we derive

$$\psi_<-\psi_>=-\sum_p b_p\cos(p\theta), \tag{A5}$$

$$\frac{1}{n^2}\frac{\partial\psi_<}{\partial r}-\frac{\partial\psi_>}{\partial r}=k\sum_p\left[a_pT_p(kR)-b_p\frac{H_p'(kR)}{H_p(kR)}\right]\cos(p\theta). \tag{A6}$$

We see that all $a_{p\neq m}$ and b_p are at least $O(\epsilon)$ by comparing the above expressions to the expansions (A2) and (A3). Thus we rewrite $a_{p\neq m}\equiv\alpha_p\epsilon+\beta_p\epsilon^2+O(\epsilon^3)$ and $b_p\equiv\mu_p\epsilon+\gamma_p\epsilon^2+O(\epsilon^3)$. In the case of TM modes $\mu_p=0$ as $(\psi_<-\psi_>)$ is at least $O(\epsilon^2)$ [33] by substituting the correspondent of Eq. (A3) into (A2).

Using (A4) we can rewrite the differences on the right-hand sides of Eqs. (A5) and (A6) as

$$\frac{\partial\psi_<}{\partial r}-\frac{\partial\psi_>}{\partial r}=k\sum_p\left[a_pS_p(kR)-b_p\frac{H_p'(kR)}{H_p(kR)}\right]\cos(p\theta), \tag{A7}$$

$$\frac{\partial^2\psi_<}{\partial r^2}-\frac{\partial^2\psi_>}{\partial r^2}=-\frac{k}{R}\sum_p[S_p(kR)+kR(n^2-1)]a_p\cos(p\theta)+\frac{k}{R}\sum_p\left[\frac{H_p'(kR)}{H_p(kR)}-\left(\frac{p^2}{kR}-kR\right)\right]b_p\cos(p\theta), \tag{A8}$$

$$\frac{1}{n^2}\frac{\partial^2\psi_<}{\partial r^2}-\frac{\partial^2\psi_>}{\partial r^2}=-\frac{k}{R}\sum_p\left[T_p(kR)+\frac{p^2}{n^2kR}(n^2-1)\right]a_p\cos(p\theta)+\frac{k}{R}\sum_p\left[\frac{H_p'(kR)}{H_p(kR)}-\left(\frac{p^2}{kR}-kR\right)\right]b_p\cos(p\theta), \tag{A9}$$

$$\frac{1}{n^2}\frac{\partial^3\psi_<}{\partial r^3}-\frac{\partial^3\psi_>}{\partial r^3}=\sum_p\left[kT_p(kR)\left(\frac{p^2+2}{R^2}-n^2k^2\right)-(n^2-1)k^3\frac{H_p'(kR)}{H_p(kR)}+\frac{3p^2}{n^2R^3}(n^2-1)\right]a_p\cos(p\theta)$$
$$-\sum_p\left[k\frac{H_p'(kR)}{H_p(kR)}\left(\frac{p^2+2}{R^2}-k^2\right)-\frac{1}{R}\left(\frac{3p^2}{R^2}-k^2\right)\right]b_p\cos(p\theta). \tag{A10}$$

When deriving the last three expressions, we have used $J_p''(z)+\frac{1}{z}J_p'(z)+(1-\frac{p^2}{z^2})J_p(z)=0$ and its derivative, which give, for example,

$$\frac{J_p''(nkR)}{J_p(nkR)}=-\frac{1}{nkR}\frac{J_p'(nkR)}{J_p(nkR)}+\left(\frac{p^2}{n^2k^2R^2}-1\right), \tag{A11}$$

$$\frac{J_p'''(nkR)}{J_p(nkR)}=\frac{J_p'(nkR)}{J_p(nkR)}\left(\frac{p^2+2}{n^2k^2R^2}-1\right)-\frac{1}{nkR}\left(\frac{3p^2}{n^2k^2R^2}-1\right). \tag{A12}$$

Next we expand the Bessel and Hankel functions around $k=k_0$. It is straightforward to see that the zeroth-order term in (A6) vanishes, which is consistent with the right-hand side of (A3). We keep the terms in Eqs. (A2) and (A3) up to order ϵ^2 in the discussion below, and Eqs. (A5)–(A10) become

$$\psi_<-\psi_>=-\sum_p(\mu_p\epsilon+\gamma_p\epsilon^2)\cos(p\theta)+O(\epsilon^3), \tag{A13}$$

$$\frac{1}{n^2}\frac{\partial\psi_<}{\partial r}-\frac{\partial\psi_>}{\partial r}=\epsilon k_0\left[k_1RT_m'(k_0R)\cos(m\theta)+\sum_{p\neq m}\alpha_pT_p(k_0R)\cos(p\theta)-\sum_p\mu_p\frac{H_p'(k_0R)}{H_p(k_0R)}\cos(p\theta)\right]$$

$$+\epsilon^2\left[k_1^2 R T_m'(k_0R)+k_0k_2RT_m'(k_0R)+\frac{1}{2}k_0k_1^2R^2T_m''(k_0R)\right]\cos(m\theta)$$
$$-\epsilon^2\sum_p\left[k_1\mu_p\frac{H_p'(k_0R)}{H_p(k_0R)}+k_0\mu_pk_1R\left(\frac{H_p'(z)}{H_p(z)}\right)'_{z=k_0R}+k_0\frac{H_p'(k_0R)}{H_p(k_0R)}\gamma_p\right]\cos(p\theta)$$
$$+\epsilon^2\sum_{p\neq m}[k_1\alpha_pT_p(k_0R)+k_0\alpha_pk_1RT_p'(k_0R)+k_0T_p(k_0R)\beta_p]\cos(p\theta)+O(\epsilon^3), \tag{A14}$$

$$\frac{\partial\psi_<}{\partial r}-\frac{\partial\psi_>}{\partial r}=k_0S_m(k_0R)\cos(m\theta)+\epsilon k_1[S_m(k_0R)+k_0RS_m'(k_0R)]\cos(m\theta)$$
$$+\epsilon k_0\left[\sum_{p\neq m}\alpha_pS_p(k_0R)-\sum_p\mu_p\frac{H_p'(k_0R)}{H_p(k_0R)}\right]\cos(p\theta)+O(\epsilon^2), \tag{A15}$$

$$\frac{\partial^2\psi_<}{\partial r^2}-\frac{\partial^2\psi_>}{\partial r^2}=-\frac{k_0}{R}[S_m(k_0R)+k_0R(n^2-1)]\cos(m\theta)+O(\epsilon^1), \tag{A16}$$

$$\frac{1}{n^2}\frac{\partial^2\psi_<}{\partial r^2}-\frac{\partial^2\psi_>}{\partial r^2}=-(n^2-1)\frac{m^2}{n^2R^2}\cos(m\theta)-\epsilon k_0k_1T_m'(k_0R)\cos(m\theta)-\epsilon\sum_{p\neq m}\left[\frac{k_0}{R}T_p(k_0R)+\frac{p^2}{n^2R^2}(n^2-1)\right]\alpha_p\cos(p\theta)$$
$$+\epsilon\sum_p\left[\frac{k_0}{R}\frac{H_p'(k_0R)}{H_p(k_0R)}-\left(\frac{p^2}{R^2}-k_0^2\right)\right]\mu_p\cos(p\theta)+O(\epsilon^2), \tag{A17}$$

$$\frac{1}{n^2}\frac{\partial^3\psi_<}{\partial r^3}-\frac{\partial^3\psi_>}{\partial r^3}=(n^2-1)\left[\frac{3m^2}{n^2R^3}-k_0^3\frac{H_m'(k_0R)}{H_m(k_0R)}\right]\cos(m\theta)+O(\epsilon^1). \tag{A18}$$

Henceforth we drop the arguments in the Bessel and Hankel functions. The first-order terms of ϵ in (A2) are then

$$-\sum_p\mu_p\epsilon\cos(p\theta)=-\epsilon f(\theta)k_0S_m\cos(m\theta), \tag{A19}$$

which gives the first-order correction in b_p:

$$\mu_p=(k_0R)S_mF_{pm}^{(1)}, \tag{A20}$$

where $F_{pm}^{(\nu)}=c_p\int_0^{2\pi}f^\nu(\theta)\cos(p\theta)\cos(m\theta)d\theta/(2\pi R^\nu)$ ($\nu=1,2$). We have dropped the superscript of $F_{pm}^{(1)}$ in the main text.

The first-order terms of ϵ in (A3) are

$$\epsilon k_0\left[T_m'k_1R\cos(m\theta)+\sum_{p\neq m}\alpha_pT_p\cos(p\theta)-\sum_p\mu_p\frac{H_p'}{H_p}\cos(p\theta)\right]=\epsilon f(\theta)\frac{m^2}{n^2R^2}(n^2-1)\cos(m\theta), \tag{A21}$$

which give

$$k_1R=\frac{1}{T_m'}\left[\frac{m^2}{n^2k_0R}(n^2-1)+k_0RS_m\frac{H_m'}{H_m}\right]F_{mm}^{(1)}, \tag{A22}$$

$$\alpha_{p\neq m}=\frac{1}{T_p}\left[\frac{m^2}{n^2k_0R}(n^2-1)+k_0RS_m\frac{H_p'}{H_p}\right]F_{pm}^{(1)}. \tag{A23}$$

Using $T_m=0$, or $nH_m'/H_m=J_m'/J_m$, and the relation

$$T_m'=\left[\frac{J_m''}{J_m}-\left(\frac{J_m'}{J_m}\right)^2\right]-\left[\frac{H_m''}{H_m}-\left(\frac{H_m'}{H_m}\right)^2\right] \tag{A24}$$
$$=-\frac{(n^2-1)m^2}{(nk_0R)^2}-\frac{H_m'}{H_m}S_m, \tag{A25}$$

Eq. (A22) is reduced to $k_1=-k_0F_{mm}^{(1)}$, which is the same as the first-order correction to TM resonances [33].

The ϵ^2 terms in (A2) are

$$-\sum_p\gamma_p\epsilon^2\cos(p\theta)=-\epsilon f(\theta)\left[\epsilon\left(k_1S_m+k_0k_1RS_m'-k_0\mu_m\frac{H_m'}{H_m}\right)\cos(m\theta)+\epsilon k_0\sum_{p\neq m}\left(\alpha_pS_p-\mu_p\frac{H_p'}{H_p}\right)\cos(p\theta)\right]$$
$$+\frac{k_0}{2R}\epsilon^2f(\theta)^2[S_m+k_0R(n^2-1)]\cos(m\theta), \tag{A26}$$

from which the second-order correction in b_p can be derived:

$$\gamma_p = \left(k_1 R S_m + k_0 k_1 R^2 S_m' - k_0 R \mu_m \frac{H_m'}{H_m}\right) F_{pm}^{(1)} + k_0 R \sum_{q\neq m} \left(\alpha_q S_q - \mu_q \frac{H_q'}{H_q}\right) F_{pq}^{(1)} - \frac{k_0 R}{2}[S_m + k_0 R(n^2-1)]F_{pm}^{(2)} \quad \text{(A27)}$$

$$= (n^2-1)(k_0R)^2\left[1 + n^2\left(\frac{H_m'}{H_m}\right)^2\right]F_{mm}^{(1)}F_{pm}^{(1)} + (n^2-1)k_0R\sum_{q\neq m}\frac{1}{T_q}\left(S_q\frac{m^2}{n^2k_0R} + \frac{k_0R}{n}S_m\frac{J_q'}{J_q}\frac{H_q'}{H_q}\right)F_{qm}^{(1)}F_{pq}^{(1)}$$

$$- \frac{k_0R}{2}[S_m + k_0R(n^2-1)]F_{pm}^{(2)}. \quad \text{(A28)}$$

The ϵ^2 terms in (A3) are

$$\epsilon^2\left[k_1^2RT_m' + k_0k_2RT_m' + \frac{1}{2}k_0k_1^2R^2T_m''\right]\cos(m\theta) + \epsilon^2\sum_{p\neq m,m'}[k_1\alpha_pT_p + k_0\alpha_pk_1RT_p' + k_0T_p\beta_p]\cos(p\theta)$$

$$-\epsilon^2\sum_p\left[k_1\mu_p\frac{H_p'}{H_p} + k_0\mu_pk_1R\left[\frac{H_p'}{H_p}\right]' + k_0\frac{H_p'}{H_p}\gamma_p\right]\cos(p\theta)$$

$$= -\epsilon f(\theta)\frac{k_0}{R}\left[-(k_1R\epsilon)T_m'\cos(m\theta) - \sum_{p\neq m}\left(T_p + \frac{p^2}{n^2k_0R}(n^2-1)\right)\alpha_p\epsilon\cos(p\theta)\right.$$

$$\left. + \sum_p\left(\frac{H_p'}{H_p} - \frac{p^2}{k_0R} + k_0R\right)\mu_p\epsilon\cos(p\theta)\right] - \frac{1}{2}\epsilon^2f(\theta)^2(n^2-1)\left[-k_0^3\frac{H_m'}{H_m} + \frac{3m^2}{n^2R^3}\right]\cos(m\theta), \quad \text{(A29)}$$

the left-hand side of which can be simplified using Eq. (A21). From the mth harmonic on both sides we obtain the second-order correction to the resonance,

$$T_m'k_2R = -\frac{1}{2}(k_1R)^2T_m'' + \gamma_m\frac{H_m'}{H_m} + \mu_mk_1R\left[\frac{H_m'}{H_m}\right]' + \left[k_1RT_m' - \frac{k_1}{k_0}\frac{m^2(n^2-1)}{n^2k_0R}\right]F_{mm}^{(1)} + \sum_{p\neq m}\left(T_p + \frac{p^2}{n^2k_0R}(n^2-1)\right)\alpha_pF_{mp}^{(1)}$$

$$- \sum_p\left(\frac{H_p'}{H_p} - \frac{p^2}{k_0R} + k_0R\right)\mu_pF_{mp}^{(1)} + \frac{1}{2}(n^2-1)\left[(k_0R)^2\frac{H_m'}{H_m} - \frac{3m^2}{n^2k_0R}\right]F_{mm}^{(2)}, \quad \text{(A30)}$$

and from the pth harmonic on both sides we obtain the second-order correction to $a_{p\neq m}$:

$$T_p\beta_p = -\alpha_pk_1RT_p' + \gamma_p\frac{H_p'}{H_p} + \mu_pk_1R\left[\frac{H_p'}{H_p}\right]' + \left[k_1RT_m' - \frac{k_1}{k_0}\frac{m^2(n^2-1)}{n^2k_0R}\right]F_{pm}^{(1)} + \sum_{q\neq m}\left(T_q + \frac{q^2}{n^2k_0R}(n^2-1)\right)\alpha_qF_{pq}^{(1)}$$

$$- \sum_q\left(\frac{H_q'}{H_q} - \frac{q^2}{k_0R} + k_0R\right)\mu_qF_{pq}^{(1)} + \frac{1}{2}(n^2-1)\left[(k_0R)^2\frac{H_m'}{H_m} - \frac{3m^2}{n^2k_0R}\right]F_{pm}^{(2)}. \quad \text{(A31)}$$

In the main text we have shown that the perturbation theory gives good agreement with the wave solutions. Here we give one simple analytical example to further confirm its validity: $f(\theta) = R$, i.e., a disk of radius $\rho = R(1+\epsilon)$ in which $F_{pm}^{(1)} = F_{pm}^{(2)} = \delta_{pm}$. The exact resonance can be easily obtained from scaling, i.e., $k = k_0R/(R+\epsilon R) \approx k_0(1-\epsilon+\epsilon^2) + O(\epsilon^3)$, which implies $k_1 = -k_0 = -k_0F_{mm}^{(1)}$, as given by Eq. (A22), and $k_2 = k_0$.

To confirm the latter, we note that Eq. (A30) takes the following form:

$$k_2RT_m' = -\frac{1}{2}(k_1R)^2T_m'' + k_1RT_m' + \gamma_m\frac{H_m'}{H_m} + \frac{1}{2}(n^2-1)\left[(k_0R)^2\frac{H_m'}{H_m} - \frac{3m^2}{n^2k_0R}\right]$$

$$+ \mu_mk_1R\left[\frac{H_p'}{H_p}\right] - \frac{k_1}{k_0}\frac{m^2(n^2-1)}{n^2k_0R} - \left(\frac{H_m'}{H_m} - \frac{m^2}{k_0R} + k_0R\right)\mu_m. \quad \text{(A32)}$$

Using

$$T_m'' = -\frac{T_m'}{k_0R} + \frac{2(n^2-1)m^2}{n^0(k_0R)^3} - 2\frac{H_m'}{H_m}S_m', \quad \text{(A33)}$$

$$\frac{H_m''(kR)}{H_m(kR)} = -\frac{1}{kR}\frac{H_m'(kR)}{H_m(kR)} + \left(\frac{m^2}{k^2R^2} - 1\right), \quad \text{(A34)}$$

the right-hand side of Eq. (A32) is reduced to k_0RT_m', indicating that $k_2 = k_0$, as we have expected. Since the cavity is still circular and the angular momentum is conserved, all $\alpha_{p\neq m}$, $\beta_{p\neq m}$ in the expansion of $\psi_<$ and $\mu_{p\neq m}$, $\gamma_{p\neq m}$ in the expansion of $\psi_>$ should be zero. Indeed this is the case as can be read off from Eqs. (A20), (A23), (A28), and (A31).

[1] *Optical Processes in Microcavities*, edited by R. K. Chang and A. J. Campillo, Advanced Series in Applied Physics (World Scientific, Singapore, 1996).
[2] *Optical Microcavities*, edited by K. J. Vahala, Advanced Series in Applied Physics (World Scientific, Singapore, 2004).
[3] A. M. Armani, R. P. Kulkarni, S. E. Fraser, R. C. Flagan, and K. J. Vahala, Science **317**, 783 (2007).
[4] F. Vollmera, S. Arnoldb, and D. Kengb, Proc. Natl. Acad. Sci. USA **105**, 20701 (2008).
[5] L. He, S. K. Özdemir, J. Zhu, W. Kim, and L. Yang, Nat. Nanotechnol. **6**, 428 (2011).
[6] A. Mekis, J. U. Nöckel, G. Chen, A. D. Stone, and R. K. Chang, Phys. Rev. Lett. **75**, 2682 (1995).
[7] J. U. Nöckel and A. D. Stone, Nature (London) **385**, 45 (1997).
[8] C. Gmachl *et al.*, Science **280**, 1556 (1998).
[9] G. D. Chern *et al.*, Appl. Phys. Lett. **83**, 1710 (2003).
[10] Y. Baryshnikov, P. Heider, W. Parz, and V. Zharnitsky, Phys. Rev. Lett. **93**, 133902 (2004).
[11] H. G. L. Schwefel *et al.*, J. Opt. Soc. Am. B **21**, 923 (2004).
[12] M. Lebental, J. Lauret, R. Hierle, and J. Zyss, Appl. Phys. Lett. **88**, 031108 (2006).
[13] J. Gao *et al.*, Appl. Phys. Lett. **91**, 181101 (2007).
[14] T. Tanaka, M. Hentschel, T. Fukushima, and T. Harayama, Phys. Rev. Lett. **98**, 033902 (2007).
[15] J. Wiersig and M. Hentschel, Phys. Rev. Lett. **100**, 033901 (2008).
[16] Q. J. Wang *et al.*, Proc. Natl. Acad. Sci. USA **107**, 22407 (2010).
[17] S. Lacey, H. Wang, D. H. Foster, and J. U. Nöckel, Phys. Rev. Lett. **91**, 033902 (2003).
[18] V. A. Podolskiy and E. E. Narimanov, Opt. Lett. **30**, 474 (2005).
[19] S. C. Creagh, Phys. Rev. Lett. **98**, 153901 (2007).
[20] S. Shinohara, T. Harayama, T. Fukushima, M. Hentschel, T. Sasaki, and E. E. Narimanov, Phys. Rev. Lett. **104**, 163902 (2010).
[21] S. C. Creagh and M. M. White, Phys. Rev. E **85**, 015201 (2012).
[22] Y. F. Xiao *et al.*, Opt. Lett. **34**, 509 (2009).
[23] Q. H. Song, L. Ge, A. D. Stone, H.Cao, J. Wiersig, J. B. Shim, J. Unterhinninghofen, W. Fang, and G. S Solomon, Phys. Rev. Lett. **105**, 103902 (2010).
[24] Q. H. Song, L. Ge, J. Wiersig, J. B. Shim, J. Unterhinninghofen, A. Eberspacher, W. Fang, G. S. Solomon, and H. Cao, Phys. Rev. A **84**, 063843 (2011).
[25] B. Redding, L. Ge, Q. Song, J. Wiersig, G. S. Solomon, and H. Cao, Phys. Rev. Lett. **108**, 253902 (2012).
[26] J. Wiersig, Phys. Rev. Lett. **97**, 253901 (2006).
[27] T. Carmon, H. G. L. Schwefel, L. Yang, M. Oxborrow, A. D. Stone, and K. J. Vahala, Phys. Rev. Lett. **100**, 103905 (2008).
[28] S.-B. Lee, J. Yang, S. Moon, S. Y. Lee, J. B. Shim, S. W. Kim, J. H. Lee, and K. An, Phys. Rev. Lett. **103**, 134101 (2009).
[29] M. Liertzer, L. Ge, A. Cerjan, A. D. Stone, H. E. Tureci, and S. Rotter, Phys. Rev. Lett. **108**, 173901 (2012).
[30] H. E. Türeci, H. G. L. Schwefel, P. Jacquod, and A. D. Stone, Prog. Opt. **47**, 75 (2005).
[31] E. E. Narimanov, G. Hackenbroich, P. Jacquod, and A. D. Stone, Phys. Rev. Lett. **83**, 4991 (1999).
[32] J. Wiersig and M. Hentschel, Phys. Rev. A **73**, 031802 (2006).
[33] R. Dubertrand, E. Bogomolny, N. Djellali, M. Lebental, and C. Schmit, Phys. Rev. A **77**, 013804 (2008).
[34] S. Ng, P. Leung, and K. Lee, J. Opt. Soc. Am. B **19**, 154 (2002).
[35] J. Lee, S. Rim, J. Cho, and C.-M. Kim, Phys. Rev. Lett. **101**, 064101 (2008).
[36] J. Wiersig, Phys. Rev. A **85**, 063838 (2012).
[37] Y. D. Chong, L. Ge, H. Cao, and A. D. Stone, Phys. Rev. Lett. **105**, 053901 (2010).
[38] W. Wan, Y. D. Chong, L. Ge, H. Noh, A. D. Stone, and H. Cao, Science **331**, 889 (2011).